ADVANCED ENERGY MATERIALS
www.advenergymat.de

Revitalizing Sulfide Solid Electrolytes for All-Solid-State Batteries: Dry-Air Exposure and Microwave-Driven Regeneration

*Boyeong Jang, Yong Bae Song, Ki Heon Baeck, Jongyoung Lee, Soon-Jae Jung, Seungwoo Choi, Hyun-Wook Lee, and Yoon Seok Jung**

Processing sulfide solid electrolytes under dry-air conditions at which certain levels of moisture are unavoidable poses challenges in the practical mass production of all-solid-state batteries (ASSBs). Herein, a facile microwave-driven regeneration method is presented for Li_6PS_5Cl (LPSCl) degraded by dry-air exposure, particularly after solvent treatment. While dry-air exposure with a dew point of −40 °C for 6 h degrades the Li^+ conductivity of wet-processed LPSCl from 3.33 to 2.55 mS cm^{-1} at 30 °C, microwave irradiation at 800 W for only 10 min restores 98.3% of the Li^+ conductivity of pristine LPSCl (3.26 mS cm^{-1}) and maintains its electron-insulating property. By contrast, conventional furnace heat treatment recovers only 83.8% of Li^+ conductivity and causes severe carbonization. Comprehensive analyses reveal that microwave heating selectively eliminates hydration layers and carbonates without inducing structural alterations or byproduct evolution. Electrochemical tests demonstrate that the microwave-regenerated LPSCl achieves performance nearly identical to the pristine LPSCl in $LiNi_{0.7}Co_{0.15}Mn_{0.15}O_2$||(Li-In) cells. Its practical applicability is further validated in $LiNi_{0.7}Co_{0.15}Mn_{0.15}O_2$||(Ag−C) pouch-type ASSBs. This rapid, scalable, and energy-efficient regeneration method can ensure consistent sulfide solid electrolyte performance, regardless of storage or transport history, enabling reliable large-scale manufacturing of ASSBs.

1. Introduction

Li argyrodites, such as Li_6PS_5Cl (LPSCl), are a representative class of sulfide solid electrolytes (SSEs), and stand out as promising candidates for all-solid-state batteries (ASSBs) owing to their cost-effective constituent elements, crystalline structures that are conducive to stable and reproducible production, versatile synthesis routes, and compatibility with solvent-based processes such as wet-milling and tape casting.[1–18]

Despite extensive progress in SSE development, their inherent chemical instability remains a major challenge for the manufacturing of ASSBs.[14,19–21] A key issue is the poor chemical stability of SSEs upon exposure to H_2O molecules.[19,22] In atmospheric air, SSEs undergo moisture-driven degradation through two primary mechanisms: i) hydrolysis, releasing toxic H_2S gas, and ii) hydration, involving H_2O adsorption onto the hydrophilic functional groups on the hydrolyzed SSE surface.[22–27] This moisture susceptibility can lead to structural and electrochemical degradation, underscoring the critical necessity for air stability control during ASSB fabrication, as well as throughout the storage and transportation of cell materials.[28] To mitigate poor moisture stability, various strategies have been developed, including substituting "hard" P with "soft" metals (e.g., Sn, Sb, and As) based on the hard and soft acid-base theory,[29–33] and employing surface treatments, such as gas-mediated treatment and hydrophobic polymer coatings.[21,34–38] However, these approaches often entail trade-offs, such as reduced ionic conductivity, compromised reduction stability, reliance on toxic or heavy elements, and increased costs.

While most laboratory-scale research on ASSBs with SSEs has been conducted within glove boxes, practical applications require processing in a dry room, where exposure to certain levels of H_2O and oxygen is unavoidable.[14,15,21,23,27,39–41] Since degradation directly affects the performance of the final cells, it is crucial to understand the underlying degradation mechanisms and devise effective strategies for stability control.[42]

B. Jang, Y. B. Song, K. H. Baeck, J. Lee, Y. S. Jung
Department of Chemical and Biomolecular Engineering
Yonsei University
Seoul 03722, Republic of Korea
E-mail: yoonsjung@yonsei.ac.kr
S.-J. Jung, S. Choi, H.-W. Lee
School of Energy and Chemical Engineering
Ulsan National Institute of Science and Technology (UNIST)
Ulsan 44919, Republic of Korea
Y. S. Jung
Department of Battery Engineering
Yonsei University
Seoul 03722, Republic of Korea

The ORCID identification number(s) for the author(s) of this article can be found under https://doi.org/10.1002/aenm.202502981

DOI: 10.1002/aenm.202502981

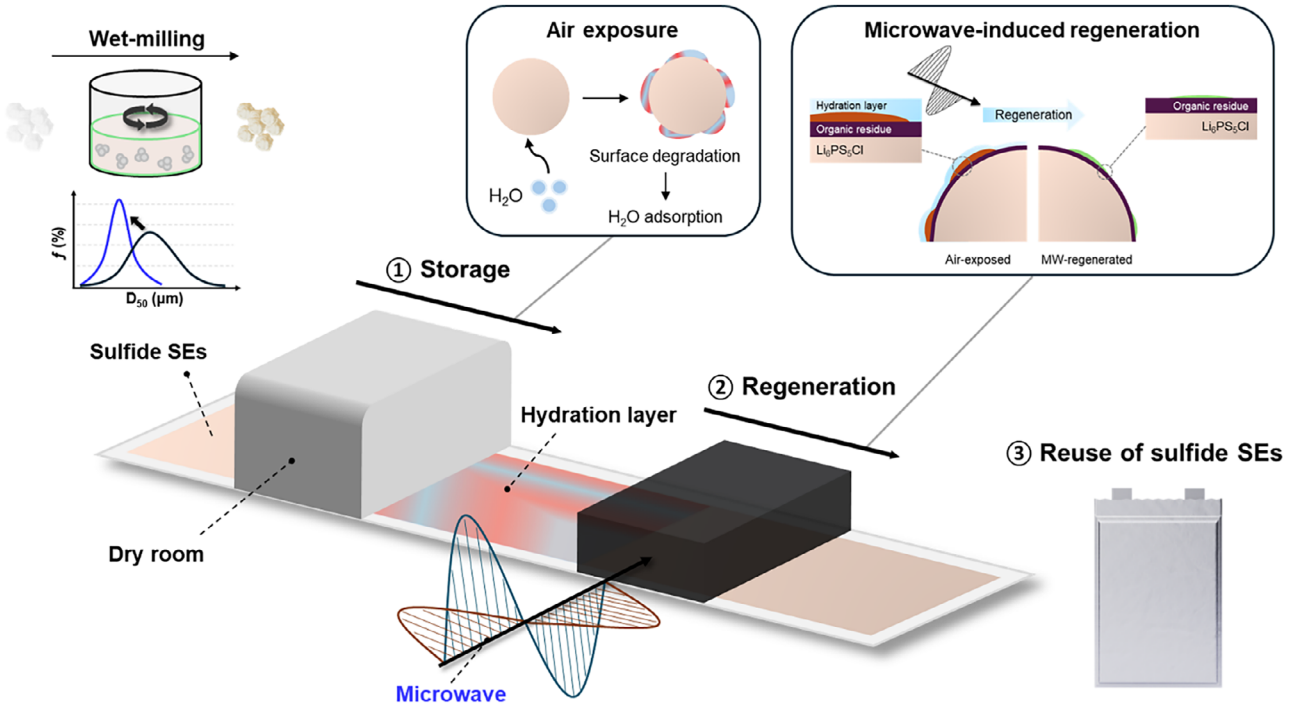

Figure 1. Schematic illustrating the microwave (MW)-driven regeneration process of dry-air-exposed sulfide solid electrolytes (SSEs) during storage under dry room conditions for all-solid-state battery (ASSB) manufacturing.

Recent studies have shown that reheating of degraded SSEs to elevated temperatures, such as 550 °C, can partially restore their ionic conductivity by removing adsorbed H_2O.[26,41,43,44] While conventional furnace-based heat treatment (HT) using electric resistance heating has been the standard method in most studies, it relies on inefficient bulk thermal diffusion, requiring substantial energy and time to achieve uniform thermal equilibrium.[44] The use of alternative energy sources, such as microwave (MW), ultraviolet, infrared (IR), and laser irradiation, has demonstrated promising potential for addressing the inefficiency and drawbacks of the conventional HT approach.[45–50] These methods leverage distinct energy sources to enable efficient energy conversion and precisely localized heating.[45] In particular, MW irradiation stands out due to its ability to selectively interact with specific materials, such as H_2O molecules and carbon, and generate thermal energy through electromagnetic energy absorption.[45,47,48]

In practice, pristine SSEs introduced into the cell manufacturing process may have undergone solvent treatment during the synthesis and/or processing stages (e.g., wet-milling processes to control the particle size).[6,14,15,51,52] Consequently, most pristine SSEs supplied by vendors likely retain residual solvents or their derivatives on their surfaces, as described in the "effects of solvent treatment on SSEs" section. The high temperatures required for the recovery of air-exposed, deteriorated SSEs can lead to the carbonization of organic residues, resulting in detrimental effects.[48,53]

Herein, we unveil a facile MW-driven method for the regeneration of SSEs, focusing on LPSCl degraded by air exposure and particularly on LPSCl subjected to solvent treatment (**Figure 1**). Through MW regeneration carried out at 800 W for 10 min, the Li^+ conductivity of solvent-treated LPSCl exposed to dry-air with a dew point of −40 °C for 6 h was recovered up to 98.3% of that of pristine LPSCl while maintaining its electron-insulating property (e^- conductivity of 5.2×10^{-9} S cm^{-1}). In stark contrast, conventional furnace HT achieved only 83.8% recovery and resulted in severe carbonization with an e^- conductivity of 6.7×10^{-5} S cm^{-1}. Complementary analyses of the chemical and structural changes in the surface and bulk regions revealed that MW irradiation effectively removed the surface hydration layer and eliminated carbonates from the dry-air-exposed LPSCl. When the MW-regenerated LPSCl was applied as the catholyte in $LiNi_{0.7}Co_{0.15}Mn_{0.15}O_2$ (NCM)||(Li-In) cells at 30 °C, its performance degradation relative to that of the cells using pristine LPSCl was negligible, highlighting the efficacy of the MW-driven regeneration method. Furthermore, its practical applicability was highlighted in $LiNi_{0.7}Co_{0.15}Mn_{0.15}O_2$||(Ag−C) pouch-type ASSBs.

2. Results and Discussion

2.1. Effects of Solvent Treatment on SSEs

The X-ray diffraction (XRD) patterns of SSEs obtained from various vendors predominantly exhibited characteristic reflections corresponding to the argyrodite phase (CIF No. 418489), with nearly no impurity peaks (Figure S1, Supporting Information). However, diffuse reflectance infrared Fourier transform spectroscopy (DRIFTS), which is sensitive to rough surfaces that induce diffuse reflection of IR beams, such as powder samples, revealed characteristic signals associated with organic compounds such as hydrocarbons (Figure S2, Supporting Information).[26] These observations suggest a prior solvent-related processing history, likely involving wet-milling processes.[52] The surfaces

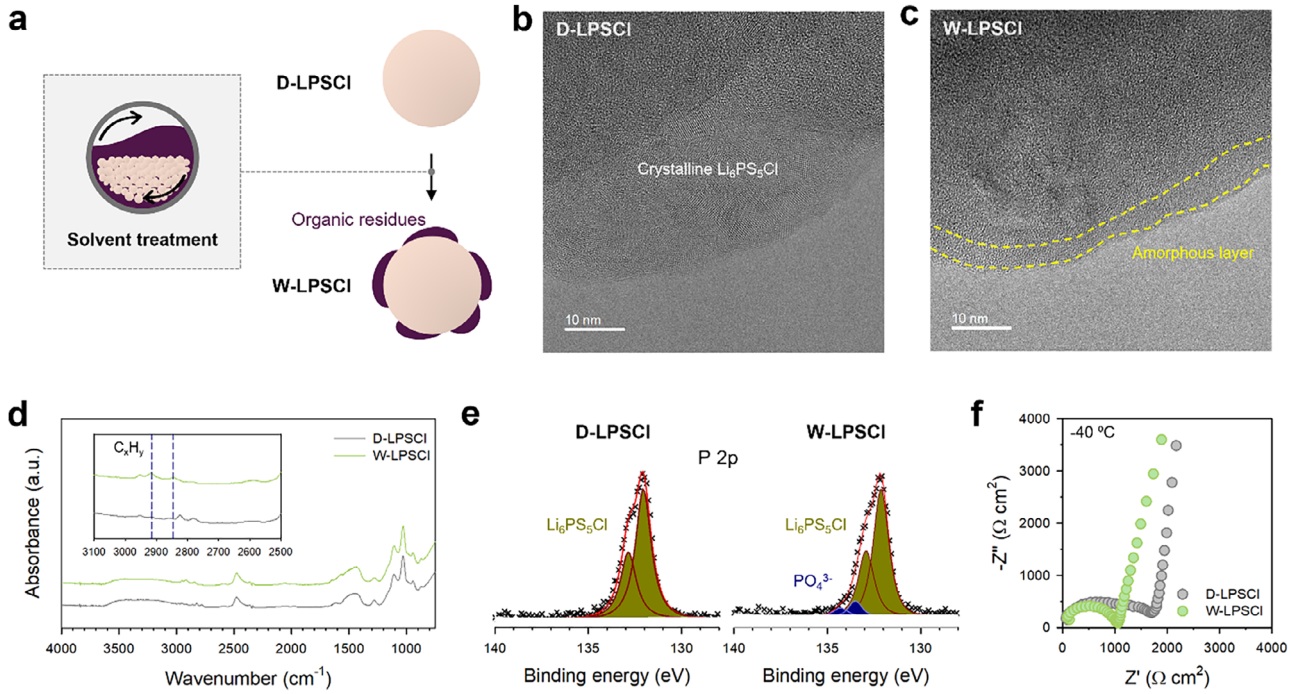

Figure 2. Characterization of dry-state LPSCl (D-LPSCl) and solvent-exposed LPSCl (W-LPSCl). a) Schematic illustrating the solvent treatment process of LPSCl. Cryo-HRTEM images of b) D-LPSCl and c) W-LPSCl. d) DRIFTS spectra, e) XPS P 2p spectra, and f) Nyquist plots of Ti|SSE|Ti symmetric cells at −40 °C for D-LPSCl and W-LPSCl.

modified during such solvent processing may exhibit various behaviors in specific chemical environments,[33,48,54,55] particularly during storage under dry-air conditions,[33] which is a scenario encountered during the manufacturing of ASSB cells.

In this context, we established an experimental design employing LPSCl as the SSE model (**Figure 2**a). Specifically, LPSCl prepared in a dry state without any prior solvent exposure is hereafter referred to as "D-LPSCl". Detailed information on the SSE samples is provided in **Table 1**. D-LPSCl was soaked in the *p*-xylene solvent, which is an inert solvent with respect to SSEs. Following the solvent treatment, the solvents were removed via vacuum filtration, and residual solvents were evaporated at 100 °C for 6 h under dynamic vacuum down at ≈7 Pa, yielding the final sample, referred to as "W-LPSCl". As expected, the XRD patterns exhibited marginal changes after the solvent treatment (Figure S3, Supporting Information). Additionally, the Li^+ conductivity of W-LPSCl at 30 °C remained nearly identical to that of D-LPSCl (3.33 vs 3.39 mS cm^{-1}) (Table 1). Similarly, solvent treatment using other SSE-compatible solvents—such as toluene, butyl butyrate, and anisole—resulted in well-retained Li^+ conductivities that were comparable to that of D-LPSCl, with minimal structural changes observed in the XRD patterns (Figure S4 and Table S1, Supporting Information). As no wet-milling process was applied, W-LPSCl retained similar particle size and morphology compared to W-LPSCl (Figure S5, Supporting Information).

Complementary analyses were conducted to further investigate the effects of the solvent treatment beyond the bulk properties. Cryogenic environments minimize beam-induced

Table 1. Characteristics of SSE samples.

Sample name	Solvent exposure	Dry-air exposure	Regeneration method		Li^+ conductivity at 30 °C [mS cm^{-1}]	e^- conductivity [S cm^{-1}]
			Furnace heating	MW heating		
D-LPSCl	–	–	–	–	3.39	1.1×10^{-9}
ex-D-LPSCl	–	O	–	–	2.55	1.1×10^{-9}
F-ex-D-LPSCl	–	O	O	–	3.86	2.3×10^{-9}
MW-ex-D-LPSCl	–	O	–	O	1.51	–
W-LPSCl	O	–	–	–	3.33	1.7×10^{-9}
ex-W-LPSCl	O	O	–	–	2.11	1.6×10^{-9}
F-ex-W-LPSCl	O	O	O	–	2.79	6.7×10^{-5}
MW-ex-W-LPSCl	O	O	–	O	3.26	5.2×10^{-9}

damage and allow the simultaneous observation of SSEs and potential organic residues.[21,33,56] Cryogenic transmission electron microscopy (cryo-TEM) analysis was performed on both D- and W-LPSCl samples, as shown in Figure 2b,c. The images revealed the formation of an amorphous layer in W-LPSCl that was absent in D-LPSCl, indicating the presence of solvent-induced surface modifications. The corresponding fast Fourier-transform (FFT) patterns are presented in Figure S6 (Supporting Information). The DRIFTS spectra consistently show distinct signals corresponding to hydrocarbon species (C_xH_y) at 2845 and 2915 cm^{-1} (Figure 2d),[26] which are absent in the spectrum of D-LPSCl. Additionally, ^1H magic-angle spinning nuclear magnetic resonance (MAS-NMR) spectroscopy confirmed the presence of hydrocarbons, as evidenced by the peak at 1.4 ppm (Figure S7, Supporting Information).[24] P 2p X-ray photoelectron spectroscopy (XPS) spectra revealed the evolution of the PO_4^{3-} species on the surface of W-LPSCl (Figure 2e).[48] These findings indicate that solvent treatment not only leaves organic residues on the surfaces but also induces chemical interactions between the SSE and organic components, leading to further chemical transformations.

Furthermore, when pelletized at 370 MPa, compared to D-LPSCl, W-LPSCl exhibited a smoother surface with fewer voids observed in the SEM top-view images (Figure S8, Supporting Information). This observation suggests that W-LPSCl is more deformable, which is likely to be due to the presence of organic residues,[33] as confirmed by DRIFTS (Figure 2d) and ^1H MAS-NMR (Figure S7, Supporting Information) results. The Li^+ conductivities of the LPSCl samples were measured using Ti|SSE|Ti Li^+-blocking symmetric cells via AC measurements. At 30 °C, the corresponding Nyquist plots displayed only straight lines with finite slopes and nearly identical x-intercept values, indicating that Li^+ conductivities were 3.39 and 3.33 mS cm^{-1} for D-LPSCl and W-LPSCl, respectively (Table 1; Figure S9, Supporting Information). However, lowering the testing temperature to −40 °C resulted in Nyquist plots that exhibited not only a low-frequency tail but also a distinct high-to-mid-frequency semicircle. This allowed the deconvolution of the grain resistance (R_g) and grain boundary resistance (R_{gb}) using the equivalent circuit model shown in Figure S10 (Supporting Information).[25,57] Notably, R_{gb} for W-LPSCl (397 Ω cm^2) was significantly lower than that of D-LPSCl (1332 Ω cm^2), while similar values of R_g were obtained for both D-LPSCl and W-LPSCl (510 Ω cm^2 for D-LPSCl and 608 Ω cm^2 for W-LPSCl) (Figure 2f; Figure S11, Supporting Information). This result is consistent with the more deformable nature of W-LPSCl, as evidenced by the SEM image (Figure S8, Supporting Information).

Solvent treatment may also influence the interactions between SSEs and air. To investigate the dry-air reactivities of D-LPSCl and W-LPSCl, both samples were exposed to dry-air for 6 h in a custom-built chamber, as shown in Figure S12 (Supporting Information). Under the dry-air condition with a dew point of −40 °C, which represents the upper limit for acceptable dry-room conditions in practical lithium-ion battery manufacturing.[58] The Li^+ conductivity at 30 °C decreased by 75% (2.55 mS cm^{-1}) for D-LPSCl and by 63% (2.11 mS cm^{-1}) for W-LPSCl (Table 1). To distinguish between the increase in the grain and grain boundary resistances, electrochemical impedance spectroscopy (EIS) measurements using Ti|SSE|Ti cells were conducted at −40 °C (Figure S13, Supporting Information). Dry-air-exposed SSE samples exhibited substantially increased grain boundary resistances compared to pristine SSEs, suggesting the formation of resistant components on the SSE surface, such as hydration layers and side reaction products.[25] The greater reduction in the ionic conductivity observed for W-LPSCl can be attributed to differences in the surface characteristics that may be driven by various interactions with dry-air, particularly between organic residues and H_2O molecules.

2.2. Regeneration of SSEs Using Microwave HT

To regenerate SSEs exposed to dry-air, conventional HT was conducted in a furnace at 550 °C for 8 h. This process eliminates the surface hydration layer and partially reconstructs crystal structures.[41] For dry-air-exposed D-LPSCl, referred to as "ex-D-LPSCl", the Li^+ conductivity at 30 °C effectively recovered from 2.55 mS cm^{-1} to 3.86 mS cm^{-1} after HT, with the regenerated sample designated as "F-ex-D-LPSCl" (Figure S14, Supporting Information; Table 1). However, when dry-air-exposed W-LPSCl, referred to as "ex-W-LPSCl", was subjected to regeneration using furnace HT, severe carbonization occurred, yielding "F-ex-W-LPSCl". While the Li^+ conductivity at 30 °C partially improved from 1.53 mS cm^{-1} to 2.79 mS cm^{-1}, the e^- conductivity at 30 °C increased significantly to 6.7×10^{-5} S cm^{-1} (**Figure 3a**; Figures S15 and S16, Supporting Information; Table 1), as evidenced by the dark-colored powders (Figure 3b). Such high e^- conductivity can detrimentally affect the electrochemical performance of the resulting ASSB cells.[48,53,59–61] This rise in the e^- conductivity is attributed to the carbonization of the organic residues in W-LPSCl, which occurs at temperatures exceeding ≈350 °C.[48,53] In a furnace with electric resistance heating, electric energy is converted into thermal energy, and heat is conducted throughout the bulk system (Figure 3c).[62] Thermal energy propagates unidirectionally from the heat source, causing the heat delivered to the sample and its temperature to vary with the distance from the source, particularly as the batch size increases. In addition, heat must propagate through the samples. The characteristics of uneven heat conduction and inefficient heat transfer that require prolonged heating can result in undesirable outcomes such as irregular crystallization of SSEs and carbonization of organic residues.

By contrast, MW irradiation directly delivers electromagnetic energy to the samples, enabling selective heating of target materials (e.g., H_2O molecules), resulting in efficient and localized heating (Figure 3d).[62] By targeting specific regions, MW heating minimizes the carbonization of organic residues.[48] During MW irradiation of dry-air-exposed SSEs, the H_2O adsorbed on their surfaces rapidly absorbs energy and evaporates (Figure 3e).[63] For regeneration, ex-W-LPSCl was subjected to MW HT at 800 W for 10 min under static vacuum, as depicted in Figure S17 (Supporting Information). Additionally, hygroscopic P_2O_5 was included to scavenge desorbed H_2O during the process. Remarkably, the Li^+ conductivity of MW-regenerated ex-W-LPSCl (referred to as "MW-ex-W-LPSCl") demonstrated exceptional retention compared to the pristine sample (W-LPSCl), achieving 98.3% retention (3.26 mS cm^{-1} at 30 °C), far surpassing the furnace-regenerated counterpart (F-ex-W-LPSCl), which showed 83.8% retention and 2.79 mS cm^{-1} (Figure 3a and Table 1).

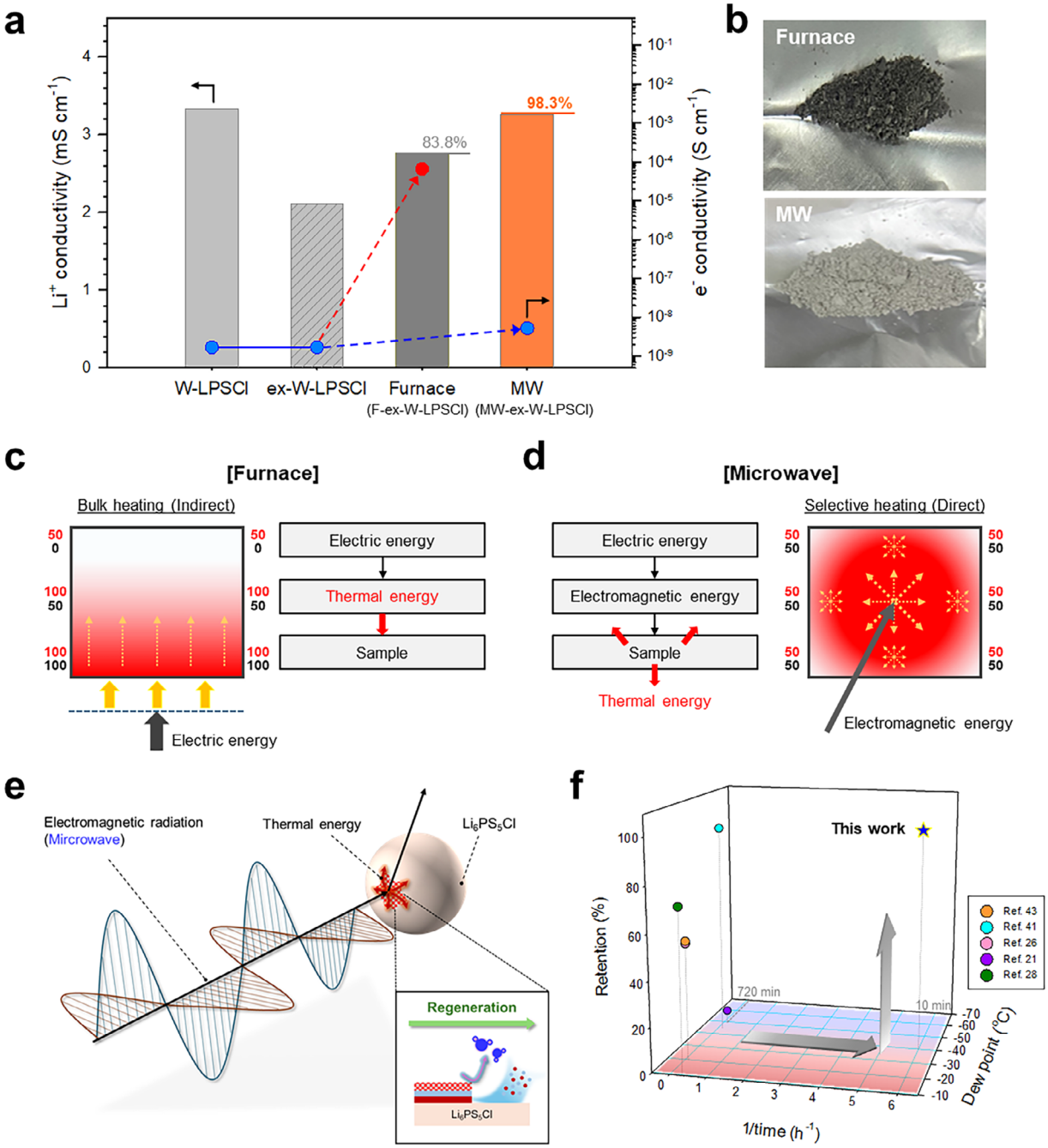

Figure 3. Comparison of the regeneration of LPSCl through furnace and MW heat treatments (HTs). a) Li^+ and e^- conductivities of pristine LPSCl (W-LPSCl), dry-air-exposed LPSCl (ex-W-LPSCl), and samples regenerated by furnace HT (F-ex-W-LPSCl) and MW HT (MW-ex-W-LPSCl). b) Optical images of furnace- and MW-regenerated LPSCl (F-ex-W-LPSCl and MW-ex-W-LPSCl). Schematic of the heat conduction model and energy conversion process in c) furnace and d) MW HTs. The box represents the target sample, while the yellow arrows on the dotted line indicate the direction of thermal conduction within the sample. The numbers next to the box show how uniformly the heat is distributed throughout the sample when a specific amount of energy is applied. e) Schematic of MW-driven regeneration of LPSCl. f) Ionic conductivity retention as a function of reciprocal time and dew point of the exposed dry-air environment, comparing previous studies with this work.

The entire MW regeneration process was achieved within only 10 min. As highlighted in Figure 3f, the combination of high Li^+ conductivity retention and rapid processing sets a remarkable benchmark for the research on the regeneration of air-exposed SSEs carried out to date (Table S2, Supporting Information). Furthermore, MW-ex-W-LPSCl exhibited a sufficiently low e^- conductivity at 5.2×10^{-9} S cm^{-1}, confirming suppressed carbonization (Figure 3a; Figures S16 and S18, Supporting Information), as also evidenced by the ivory-colored powders (Figure 3b).

2.3. Mechanism of MW-Driven Regeneration

To investigate the underlying mechanism of MW regeneration, comprehensive analyses were conducted on the pristine, dry-air-exposed, and MW-heated SSE samples. With the exception of the formation of minor impurities corresponding to Li_2S, the XRD patterns presented in **Figure 4a** do not reveal any notable structural changes upon MW regeneration. Consistently, the Raman spectra in Figure 4b show that the bands at 425 cm^{-1}, corresponding to PS_4^{3-},[26] remained unchanged both dry-air exposure and MW HT, indicating negligible alterations in the bulk structures of LPSCl. The cryo-HRTEM images revealed the presence of an amorphous layer in ex-W-LPSCl that partially disappeared after MW regeneration (Figure 4c,d; Figure S19, Supporting Information). The corresponding FFT patterns are presented in Figure S20 (Supporting Information). Energy-dispersive X-ray spectroscopy (EDXS) line mapping further confirmed a strong oxygen signal on the surface of ex-W-LPSCl (Figure 4e,f; Figure S21, Supporting Information), which was significantly reduced in MW-ex-W-LPSCl, indicating the removal of oxygen-containing species upon MW heating. These surface compositional changes were also reflected in electrochemical behavior. While R_{gb} decreased from 3648 Ω cm^2 to 1960 Ω cm^2, R_g remained largely unchanged (Figure S22, Supporting Information). These findings highlight that MW regeneration primarily affects the surface rather than the bulk, prompting us to focus on the analysis of surface characteristics.

DRIFTS measurements, which probe the surface chemistry of powder samples,[26] revealed distinct changes with MW regeneration, as presented in **Figure 5a**; the spectra exhibited strong signals of adsorbed H_2O at 1615 cm^{-1} and 3000–3600 cm^{-1} (-OH group) for the dry-air-exposed samples (ex-W-LPSCl).[26,28] These signals disappeared after MW regeneration, indicating the effective removal of adsorbed H_2O. Additionally, peaks at 860, 1420, and 1480 cm^{-1}, corresponding to Li_2CO_3, were also eliminated after MW regeneration.[26,28] Consistently, thermogravimetric analysis-mass spectrometry (TGA-MS) results in Figure S23 (Supporting Information) show a substantial decrease in the mass signals of H_2O and CO_2 in MW-ex-W-LPSCl compared to ex-W-LPSCl, further supporting the effectiveness of MW regeneration.[41] However, P 2p XPS spectra (Figure 5b) revealed that the PO_4^{3-} impurity species remained in the sample after MW regeneration.[48] This contrasting behavior may be attributed to the volatility of Li_2CO_3 at elevated temperatures, as reflected by CO_2 evolution starting at ≈300 °C in the TGA-MS results (Figure S23, Supporting Information), whereas phosphate species remained thermally intact.[64] Specifically, localized MW-induced heating likely facilitated the elimination of Li_2CO_3. Furthermore, O K-edge soft X-ray absorption spectroscopy, which is highly surface-specific (≈10 nm), provided complementary information. As shown in Figure 5c, the surface of ex-W-LPSCl was predominantly covered with Li_2CO_3.[65] After MW regeneration, the Li_2CO_3 peaks decreased drastically, and signals corresponding to Li_3PO_4 emerged, in full agreement with the XPS results (Figure 5b). Similarly, a reduction in the peak for Li_2CO_3 and the appearance of a peak for Li_3PO_4 were observed in the O K-edge soft XAS results for the MW-regenerated MW-ex-D-LPSCl (Figure S24, Supporting Information). However, the DRIFTS analysis of MW-ex-D-LPSCl revealed the persistence of Li_2CO_3 (Figure S25, Supporting Information),[26,28] indicating inefficient removal of surface Li_2CO_3, which reflects the influence of solvent treatment on the evolution of the surface.

The mechanism of the MW regeneration of ex-W-LPSCl, as deduced from the comprehensive analysis, is summarized in Figure 5d. Upon exposure to dry-air, Li_2CO_3 is formed on the surface, accompanied by H_2O adsorption. The MW irradiation of the dry-air-exposed samples effectively removed the hydration layer and Li_2CO_3, whereas minor amounts of Li_3PO_4 remained on the surface. As shown in Table S1 (Supporting Information), LPSCl samples treated with different solvents exhibited varying degrees of Li^+ conductivity retention. This suggests that the mechanisms activated by MW irradiation may differ depending on the solvent type, residual form of organic materials, and/or their interactions with SSEs. Although the main results were obtained under the optimized conditions for xylene-treated W-LPSCl, the optimal MW activation conditions may vary with the surface characteristics of each SSE, offering the potential for more precise control over the selective heating-based MW regeneration effect.

2.4. ASSBs Using MW-Regenerated SSEs

As illustrated in **Figure 6a**, SSEs stored in a dry-air atmosphere can be seamlessly integrated into cell production. At this stage, any degradation incurred during storage or transportation can be effectively revitalized through the MW regeneration process performed immediately prior to cell assembly. This strategy ensures consistent ASSB performance regardless of the storage or transport history of the SSE stock. To validate the potential of the strategy, the electrochemical performance of the MW-ex-W-LPSCl was evaluated. In cyclic voltammetry (CV) tests carried out using (sample-C)||(Li-In) cells at 0.1 mV s^{-1} and 30 °C, MW-regenerated samples exhibited profiles comparable to that of the pristine sample (Figure S26, Supporting Information). Furthermore, MW-ex-W-LPSCl was used as the catholyte in NCM||(Li-In) ASSB half-cells at 30 °C. The first-cycle charge-discharge voltage profiles at 0.1C, shown in Figure 6b, revealed comparable reversible capacities for cells with pristine W-LPSCl and MW-ex-W-LPSCl (166.6 and 167.0 mA h g^{-1}, respectively) and similar initial Coulombic efficiencies (ICEs) (79.9% and 79.2%, respectively). Additionally, the rate capabilities presented in Figure 6c confirm the comparable performances of the two samples.

For a demonstration of the feasibility of this strategy in practical ASSB cell fabrication, SSE regeneration using MW was applied to pouch-type ASSB full cells (Figure 6d). Sheet-type NCM cathodes were fabricated via a dry process utilizing ex-W-LPSCl or MW-ex-W-LPSCl as catholytes with polytetrafluoroethylene (PTFE) as the binder. Ag–C layers were employed as Li-reservoir-free anodes, corresponding to a configuration conventionally referred to as an initially anodeless system.[3] The assembled NCM||(Ag–C) pouch cells were tested at 60 °C under an operating pressure of 5 MPa. Notably, the cell utilizing MW-ex-W-LPSCl exhibits 91.7% capacity retention after 100 cycles, whereas the ex-W-LPSCl cell exhibits severe capacity degradation, showing only 41.0% capacity retention over the same period (Figure 6e; Figure S27, Supporting Information). These results

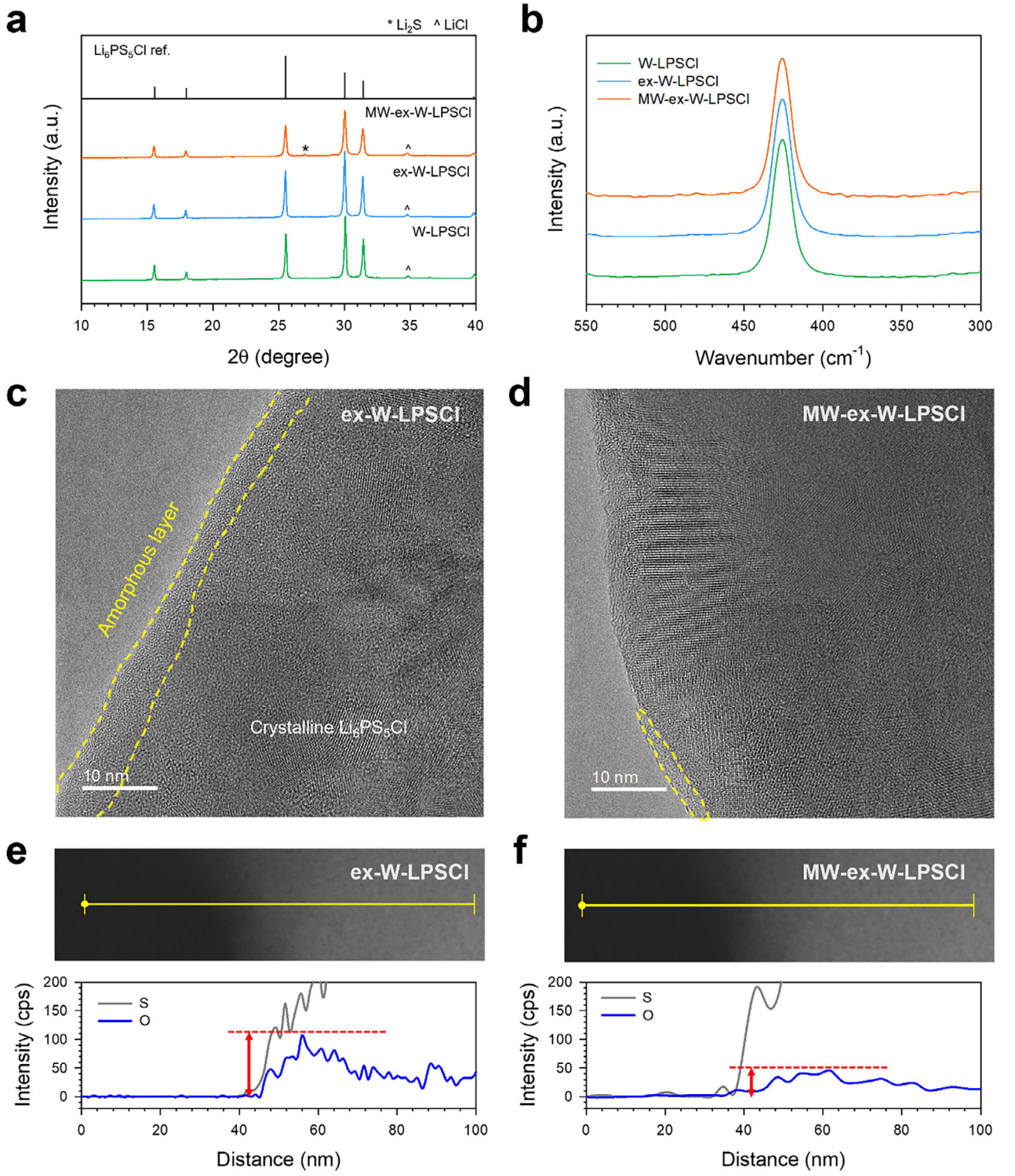

Figure 4. Characterization of LPSCl in pristine (W-LPSCl), dry-air-exposed (ex-W-LPSCl), and MW-regenerated (MW-ex-W-LPSCl) states. a) XRD patterns, b) Raman spectra. Cryo-HRTEM images of c) ex-W-LPSCl and d) MW-ex-W-LPSCl. EDXS line scan results of the surface regions along the yellow lines in panels e) for ex-W-LPSCl and f) MW-ex-W-LPSCl.

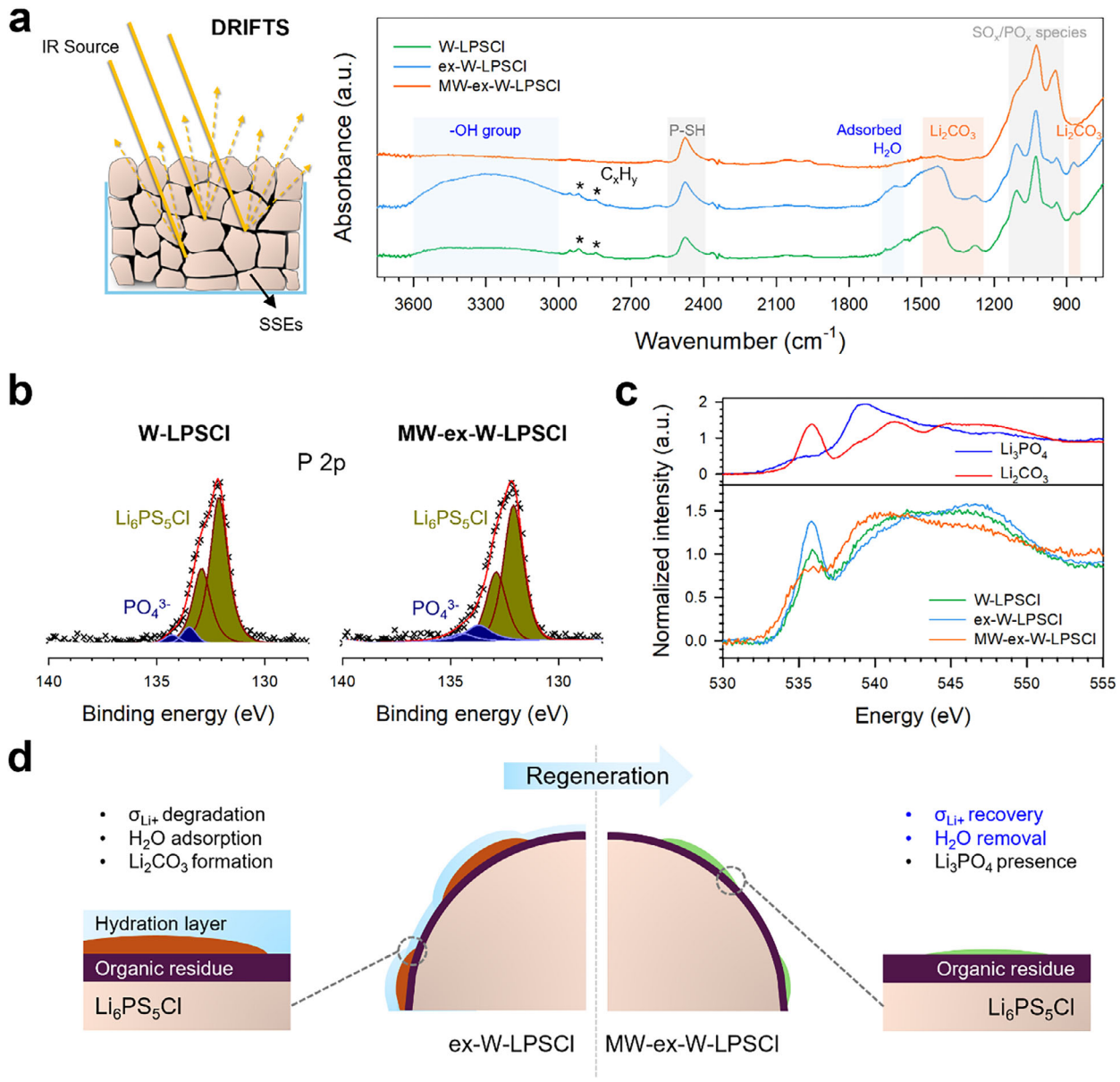

Figure 5. Surface characterization of LPSCl in pristine (W-LPSCl), dry-air-exposed (ex-W-LPSCl), and MW-regenerated (MW-ex-W-LPSCl) states. a) DRIFTS spectra with a schematic of the DRIFTS setup. b) XPS P 2p spectra of pristine and MW-regenerated LPSCl. c) O K-edge soft XAS spectra for pristine, dry-air-exposed, and MW-regenerated LPSCl, along with those for Li_3PO_4 and Li_2CO_3. d) Schematic of surface chemistry evolution during MW regeneration of LPSCl.

highlight the necessity and effectiveness of MW-induced regeneration in mitigating air-exposure-induced degradation of SSEs in practical applications.

3. Conclusion

In summary, we demonstrated a highly efficient MW-driven regeneration method for SSEs, specifically for LPSCl degraded by dry-air exposure, with a particular focus on LPSCl subjected to solvent treatment processes. MW regeneration at 800 W for 10 min effectively restored 98.3% of the Li^+ conductivity of solvent-treated LPSCl exposed to dry-air (dew point of −40 for 6 h) while preserving its e^--insulating properties. This performance far exceeds that achieved via conventional furnace HT, which restores only 83.8% of the Li^+ conductivity and causes significant carbonization, leading to a detrimental increase in e^- conductivity. Comprehensive analyses of the surface and bulk regions using XRD, Raman spectroscopy, DRIFTS, elemental analysis, ^1H MAS-NMR, XPS, O K-edge XAS, and TGA-MS revealed that MW irradiation selectively and efficiently removed surface hydration layers and carbonates while minimizing structural alterations and undesirable byproducts. Furthermore, MW-regenerated LPSCl demonstrated excellent electrochemical performance when applied as a catholyte in NCM||(Li-In) cells, achieving

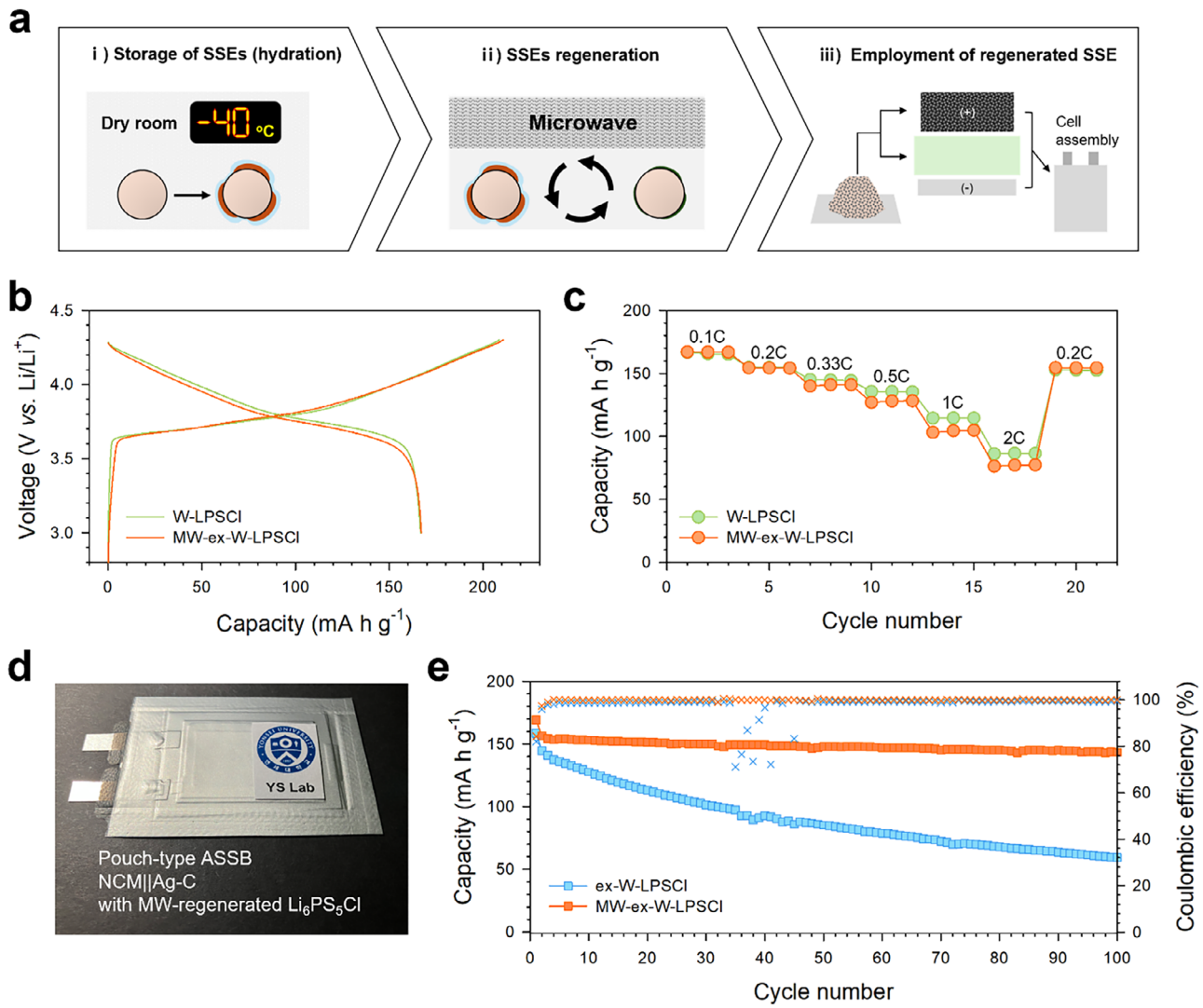

Figure 6. Electrochemical performance of ASSBs employing MW-regenerated LPSCl (MW-ex-W-LPSCl). a) Schematic illustrating the integration of MW-driven regeneration into the ASSB manufacturing process. b) First-cycle charge-discharge voltage profiles at 0.1C and c) rate capabilities of NCM||(Li-In) all-solid-state half-cells at 30 °C employing pristine and MW-regenerated LPSCl. d) Photograph of NCM||(Ag–C) ASSB pouch cell utilizing MW-regenerated LPSCl and e) corresponding cycle performance of cells at 0.5C using dry-air-exposed and MW-regenerated LPSCl at 60 °C and 5 MPa.

results nearly identical to those of cells utilizing pristine LPSCl. The practical applicability of MW-regenerated LPSCl was further validated in NCM||(Ag–C) pouch-type ASSB full cells. These findings underscore the practical potential of MW regeneration for ensuring consistent SSE performance, particularly in scenarios involving air exposure during storage or transportation. We believe that the MW regeneration strategy offers a rapid, scalable, and energy-efficient solution to address performance degradation and ensure high-performance ASSBs, while minimizing processing complexity.

4. Experimental Section

Material Preparation: To prepare W-LPSCl (solvent-treated LPSCl powders), D-LPSCl (LPSCl powders (POSCO JK Solid Solution Co.) prepared in a dry state) was soaked in p-xylene (anhydrous, ≥99%, Sigma Aldrich). The solvent was subsequently removed via vacuum filtration, followed by the evaporation of residual solvent at 100 °C for 6 h under dynamic vacuum down to ≈7 Pa. To expose the samples to dry-air conditions with a dew point of −40 °C, powders (250 mg) were placed in a custom-built chamber for 6 h. The dew point inside the custom-built chamber was maintained within ±1 °C using a cooling dehumidifier. After exposure, the samples were transferred to an Ar-filled glove box using an airtight desiccator to prevent contamination. For the regeneration of ex-LPSCl (dry-air-exposed LPSCl), the powder (120 mg) was subjected to HT using either a furnace or MW under static vacuum. Furnace HT was performed at 550 °C for 8 h at a heating rate of 5 °C min^{-1}. The MW HT was conducted at 800 W for 10 min in a customized microwave oven under manual power control. P_2O_5 was employed as the hygroscopic scavenger to trap the moisture evaporated from the ex-LPSCl powder.

Material Characterization: Structural characterization of SSEs was performed by powder XRD measurements using a Rigaku MiniFlex600 with Cu-Kα radiation (λ = 1.5406 Å) at 40 kV and 15 mA. The XRD measurements were conducted using an airtight container with a Be window to

prevent exposure to air. IR spectroscopy was performed using a compact DRIFTS system (ALPHA II with a DRIFTS module, Bruker, Germany) inside an Ar-filled glove box. The powders were tapped into an Au-coated cup and irradiated with an IR beam. For cryo-TEM measurements, the samples were loaded onto a lacey Cu grid. To avoid air exposure, a double-tilt LN2 atmosphere defense holder (Mel-Build) with a vacuum transfer capability was employed. Cryo-TEM was performed using a JEM-2100F (JEOL) instrument operating at an acceleration voltage of 200 kV. Solid-state ^{31}P MAS NMR spectra were acquired using a Bruker AVANCE II+ 400 MHz NMR system (KBSI Seoul Western Center). XPS measurements were performed using a K-Alpha+ instrument (ThermoFisher Scientific) with a monochromatic Al Kα source (1486.6 eV) at 12 kV and 3 mA. The samples were mounted on a sample holder in an Ar-filled glove box and transferred to the XPS instrument without exposure to air. SEM images were obtained using a CrossBeam 540 microscope (Zeiss). The sample specimens were stored and transported using an air-isolation system holder to avoid exposure to ambient air. Raman spectra were recorded with a LabRAM Arimis instrument (Horiba Jobin Yvon) using an Ar-ion laser beam at an excitation wavelength of 514 nm. For TGA-MS measurements, an STA 409 PC Simultaneous Thermal Analyzer coupled with a QMS403 C Mass Spectrometer was used. Samples (50 mg) were placed in Al_2O_3 pans and loaded within 1 min to minimize air exposure. All measurements were conducted in an Ar atmosphere, with the temperature scanned from 30 to 600 °C at a rate of 10 °C min^{-1}. O K-edge XAS spectra were collected at the 10D beamline of the Pohang Accelerator Laboratory (PAL) in the total-electron-yield mode.

Electrochemical Characterization: The ionic conductivities were measured using the AC impedance method with Ti|SSE|Ti symmetric cells. Pellets with a diameter of 6 mm and a mass of 30 mg were prepared at 370 MPa. The EIS data were recorded at an amplitude of 10 mV and a frequency range of 10 mHz to 7 MHz using a VMP3 (Bio-Logic). The e^- conductivities of the SSEs were determined through DC polarization measurements carried out on the pellets with an applied voltage of 1.0 V for 30 min. To determine the ionic conductivity of the furnace-regenerated LPSCl, tri-layer symmetric cells (Li|LPSCl (200 mg)|Li) and five-layer symmetric cells (Li|LPSCl (100 mg)|SSE (70 mg)|LPSCl (100 mg)|Li) were fabricated. Cell resistances were also measured using CV at a scan rate of 0.1 mV s^{-1}, and the obtained results were supported by EIS measurements. (SSE-C)||(Li-In) cells were fabricated for CV measurements. An SSE and Super C65 mixture with a weight ratio of 10:1 was used as the working electrode. The LPSCl layer served as the separating SSE layer, whereas the Li-In electrode acted as the counter/reference electrode. A $LiNbO_3$-coated NCM powder was used in this study. Composite electrodes were prepared by mixing NCM, SSE, and Super C65 in a weight ratio of 70:30:3 using a mortar and pestle. As a counter/reference electrode, $Li_{0.5}In$ (nominal composition) powder was prepared by mixing Li powder (FMC Lithium Corp.) and In powder (Sigma-Aldrich, 99%). The cell assemblies were prepared in a poly(aryl-ether-ether-ketone) mold with a diameter of 13 mm using two Ti rods as the current collectors. The SSE powders (150 mg) were pre-pelletized, after which the as-prepared NCM electrode (15 mg) and Li-In electrode (75 mg) were placed on each side of the SSE layer. The assembled cells were then pressed at 370 MPa. All NCM||(Li-In) cells were cycled between 3.0 and 4.3 V (vs Li/Li$^+$) at 30 °C. For the preparation of NCM||(Ag–C) pouch cells, NCM electrodes were prepared via a dry process using a mixture of NCM, SSE (ex-W-LPSCl or MW-ex-W-LPSCl), vapor-grown carbon fiber (VGCF), and PTFE in a weight ratio of 70.0:27.7:2.0:0.3. The resulting electrode had a mass loading of $\approx$10 mg$_{NCM}$ cm^{-2}. The LPSCl film (100 µm) was prepared via a wet-slurry method using a slurry mixture of LPSCl and nitrile-butadiene rubber (NBR) in a weight ratio of 97:3. The Ag–C interlayer, composed of Ag nanopowder, Super C65, and poly(vinylidene fluoride) in a weight ratio of 23:67:10, was prepared by a wet-slurry method. For the cell assembly, the NCM cathode, LPSCl film, and Ag-C interlayer were stacked sequentially and vacuum-sealed using Al pouch films. The assembled stack was then pressed under isostatic pressure at 450 MPa and 80 °C, resulting in 2.5 × 1.6 cm^2 pouch cells with an areal capacity of 2.0 mA h cm^{-2}. Electrochemical testing was carried out by cycling between 2.50 and 4.25 V at 5 MPa and 60 °C.

Supporting Information

Supporting Information is available from the Wiley Online Library or from the author.

Acknowledgements

B.J. and Y.B.S. contributed equally to this work. This work was supported by the National Research Foundation of Korea (NRF) grant funded by the Korea Government (MSIT) (No. RS-2024-00343349) and the Technology Innovation Program (No. 20007045 and RS-2025-02413378) funded by the Ministry of Trade, Industry & Energy (MOTIE, Korea). Experiments at PAL were supported in part by MSIT (2024-3rd-10D-018, Accelerator Application Support Project) and POSTECH.

Conflict of Interest

The authors declare no conflict of interest.

Data Availability Statement

The data that support the findings of this study are available in the supplementary material of this article.

Keywords

air-stability, all-solid-state batteries, microwaves, regeneration, solvent treatment, sulfide solid electrolytes

Received: June 1, 2025
Revised: August 6, 2025
Published online:

[1] J. Janek, W. G. Zeier, *Nat. Energy* **2016**, *1*, 16141.
[2] R. Schmuch, R. Wagner, G. Hörpel, T. Placke, M. Winter, *Nat. Energy* **2018**, *3*, 267.
[3] Y.-G. Lee, S. Fujiki, C. Jung, N. Suzuki, N. Yashiro, R. Omoda, D.-S. Ko, T. Shiratsuchi, T. Sugimoto, S. Ryu, J. H. Ku, T. Watanabe, Y. Park, Y. Aihara, D. Im, I. T. Han, *Nat. Energy* **2020**, *5*, 299.
[4] Y. Kato, S. Hori, T. Saito, K. Suzuki, M. Hirayama, A. Mitsui, M. Yonemura, H. Iba, R. Kanno, *Nat. Energy* **2016**, *1*, 16030.
[5] X. Gao, B. Liu, B. Hu, Z. Ning, D. S. Jolly, S. Zhang, J. Perera, J. Bu, J. Liu, C. Doerrer, E. Darnbrough, D. Armstrong, P. S. Grant, P. G. Bruce, *Joule* **2022**, *6*, 636.
[6] Y. B. Song, K. H. Baeck, H. Kwak, H. Lim, Y. S. Jung, *Adv. Energy Mater.* **2023**, *13*, 2301142.
[7] H. Kwak, S. Wang, J. Park, Y. Liu, K. T. Kim, Y. Choi, Y. Mo, Y. S. Jung, *ACS Energy Lett.* **2022**, *7*, 1776.
[8] H.-J. Deiseroth, S.-T. Kong, H. Eckert, J. Vannahme, C. Reiner, T. Zaiß, M. Schlosser, *Angew. Chem., Int. Ed.* **2008**, *47*, 755.
[9] A. Miura, N. C. Rosero-Navarro, A. Sakuda, K. Tadanaga, N. H. H. Phuc, A. Matsuda, N. Machida, A. Hayashi, M. Tatsumisago, *Nat. Rev. Chem.* **2019**, *3*, 189.
[10] L. Zhou, N. Minafra, W. G. Zeier, L. F. Nazar, *Acc. Chem. Res.* **2021**, *54*, 2717.
[11] K. Jun, Y. Chen, G. Wei, X. Yang, G. Ceder, *Nat. Rev. Mater.* **2024**, *9*, 887.
[12] Z. Liu, T. Zinkevich, S. Indris, X. He, J. Liu, W. Xu, J. Bai, S. Xiong, Y. Mo, H. Chen, *Inorg. Chem.* **2020**, *59*, 226.

[13] D. H. Kim, D. Y. Oh, K. H. Park, Y. E. Choi, Y. J. Nam, H. A. Lee, S.-M. Lee, Y. S. Jung, *Nano Lett.* **2017**, *17*, 3013.
[14] K. H. Park, Q. Bai, D. H. Kim, D. Y. Oh, Y. Zhu, Y. Mo, Y. S. Jung, *Adv. Energy Mater.* **2018**, *8*, 1800035.
[15] Y. J. Nam, D. Y. Oh, S. H. Jung, Y. S. Jung, *J. Power Sources* **2018**, *375*, 93.
[16] K. T. Kim, J.-S. Kim, K. H. Baeck, J. S. Kim, J. Park, S. Bong, Y. J. Park, Y. B. Song, C. Park, S.-J. Jung, H.-W. Lee, K. Lee, J. H. Song, S. Lee, D.-H. Seo, Y. S. Jung, *Adv. Mater.* **2025**, *37*, 2416816.
[17] X. Su, X.-P. Xu, Z.-Q. Ji, J. Wu, F. Ma, L.-Z. Fan, *Electrochem. Energy Rev.* **2024**, *7*, 2.
[18] S. Zhang, J. Ma, S. Dong, G. Cui, *Electrochem. Energy Rev.* **2023**, *6*, 4.
[19] Y. Nikodimos, C.-J. Huang, B. W. Taklu, W.-N. Su, B. J. Hwang, *Energy Environ. Sci.* **2022**, *15*, 991.
[20] J. Ruhl, L. M. Riegger, M. Ghidiu, W. G. Zeier, *Adv. Energy Sustainability Res.* **2021**, *2*, 2000077.
[21] K. T. Kim, J. Woo, Y.-S. Kim, S. Sung, C. Park, C. Lee, Y. J. Park, H.-W. Lee, K. Park, Y. S. Jung, *Adv. Energy Mater.* **2023**, *13*, 2301600.
[22] H. Muramatsu, A. Hayashi, T. Ohtomo, S. Hama, M. Tatsumisago, *Solid State Ionics* **2011**, *182*, 116.
[23] H. Tsukasaki, H. Sano, K. Igarashi, A. Wakui, T. Yaguchi, S. Mori, *J. Power Sources* **2022**, *524*, 231085.
[24] Y. Morino, H. Sano, T. Takahashi, N. Miyashita, A. Sakuda, A. Hayashi, *J. Phys. Chem. C* **2023**, *127*, 13616.
[25] Y. Morino, H. Sano, S. Kawaguchi, S. Hori, A. Sakuda, T. Takahashi, N. Miyashita, A. Hayashi, R. Kanno, *J. Phys. Chem. C* **2023**, *127*, 18678.
[26] Y. Morino, H. Sano, K. Kawamoto, K.-i. Fukui, M. Takeuchi, A. Sakuda, A. Hayashi, *Solid State Ionics* **2023**, *392*, 116162.
[27] P. Naillou, A. Boulineau, E. De Vito, R. Ramos, P. Azaïs, *ACS Appl. Mater. Interfaces* **2024**, *16*, 53855.
[28] L. H. Adem, B. N. Olana, B. W. Taklu, B. D. Dandena, G. G. Serbessa, B.-J. Hwang, S. D. Lin, *Electrochim. Acta* **2024**, *498*, 144622.
[29] G. Sahu, Z. Lin, J. Li, Z. Liu, N. Dudney, C. Liang, *Energy Environ. Sci.* **2014**, *7*, 1053.
[30] Z. Yu, S.-L. Shang, J.-H. Seo, D. Wang, X. Luo, Q. Huang, S. Chen, J. Lu, X. Li, Z.-K. Liu, D. Wang, *Adv. Mater.* **2017**, *29*, 1605561.
[31] H. Kwak, K. H. Park, D. Han, K.-W. Nam, H. Kim, Y. S. Jung, *J. Power Sources* **2020**, *446*, 227338.
[32] F. Zhao, S. H. Alahakoon, K. Adair, S. Zhang, W. Xia, W. Li, C. Yu, R. Feng, Y. Hu, J. Liang, X. Lin, Y. Zhao, X. Yang, T.-K. Sham, H. Huang, L. Zhang, S. Zhao, S. Lu, Y. Huang, X. Sun, *Adv. Mater.* **2021**, *33*, 2006577.
[33] J. Woo, Y. B. Song, H. Kwak, S. Jun, B. Y. Jang, J. Park, K. T. Kim, C. Park, C. Lee, K.-H. Park, H.-W. Lee, Y. S. Jung, *Adv. Energy Mater.* **2023**, *13*, 2203292.
[34] W. D. Jung, M. Jeon, S. S. Shin, J.-S. Kim, H.-G. Jung, B.-K. Kim, J.-H. Lee, Y.-C. Chung, H. Kim, *ACS Omega* **2020**, *5*, 26015.
[35] Z. Yu, S.-L. Shang, K. Ahn, D. T. Marty, R. Feng, M. H. Engelhard, Z.-K. Liu, D. Lu, *ACS Appl. Mater. Interfaces* **2022**, *14*, 32035.
[36] Y. Jin, Q. He, G. Liu, Z. Gu, M. Wu, T. Sun, Z. Zhang, L. Huang, X. Yao, *Adv. Mater.* **2023**, *35*, 2211047.
[37] X. Yang, X. Gao, M. Jiang, J. Luo, J. Yan, J. Fu, H. Duan, S. Zhao, Y. Tang, R. Yang, R. Li, J. Wang, H. Huang, C. Veer Singh, X. Sun, *Angew. Chem., Int. Ed.* **2023**, *62*, 202215680.
[38] X. Zhang, X. Li, S. Weng, S. Wu, Q. Liu, M. Cao, Y. Li, Z. Wang, L. Zhu, R. Xiao, D. Su, X. Yu, H. Li, L. Chen, Z. Wang, X. Wang, *Energy Environ. Sci.* **2023**, *16*, 1091.
[39] J. Schnell, T. Günther, T. Knoche, C. Vieider, L. Köhler, A. Just, M. Keller, S. Passerini, G. Reinhart, *J. Power Sources* **2018**, *382*, 160.
[40] J. Schnell, H. Knörzer, A. J. Imbsweiler, G. Reinhart, *Energy Technol.* **2020**, *8*, 1901237.
[41] Y.-T. Chen, M. A. T. Marple, D. H. S. Tan, S.-Y. Ham, B. Sayahpour, W.-K. Li, H. Yang, J. B. Lee, H. J. Hah, E. A. Wu, J.-M. Doux, J. Jang, P. Ridley, A. Cronk, G. Deysher, Z. Chen, Y. S. Meng, *J. Mater. Chem. A.* **2022**, *10*, 7155.
[42] R. Chen, Q. Li, X. Yu, L. Chen, H. Li, *Chem. Rev.* **2020**, *120*, 6820.
[43] H. Sano, Y. Morino, A. Yabuki, S. Sato, N. Itayama, Y. Matsumura, M. Iwasaki, M. Takehara, T. Abe, Y. Ishiguro, T. Takahashi, N. Miyashita, A. Sakuda, A. Hayashi, *Electrochemistry* **2022**, *90*, 037012.
[44] C. Yu, S. Ganapathy, J. Hageman, L. van Eijck, E. R. H. van Eck, L. Zhang, T. Schwietert, S. Basak, E. M. Kelder, M. Wagemaker, *ACS Appl. Mater. Interfaces* **2018**, *10*, 33296.
[45] X. Hu, D. Zuo, S. Cheng, S. Chen, Y. Liu, W. Bao, S. Deng, S. J. Harris, J. Wan, *Chem. Soc. Rev.* **2023**, *52*, 1103.
[46] V. C. Wu, H. A. Evans, R. Giovine, M. B. Preefer, J. Ong, E. Yoshida, P.-E. Cabelguen, R. J. Clément, *Adv. Energy Mater.* **2023**, *13*, 2203860.
[47] C. Wang, W. Ping, Q. Bai, H. Cui, R. Hensleigh, R. Wang, A. H. Brozena, Z. Xu, J. Dai, Y. Pei, C. Zheng, G. Pastel, J. Gao, X. Wang, H. Wang, J.-C. Zhao, B. Yang, X. Zheng, J. Luo, Y. Mo, B. Dunn, L. Hu, *Science* **2020**, *368*, 521.
[48] B. Jang, J. Woo, Y. B. Song, H. Kwak, J. Park, J. S. Kim, H. Lim, Y. S. Jung, *Energy Storage Mater.* **2024**, *65*, 103154.
[49] R. Li, S. Yuan, W. Zhang, H. Zheng, W. Zhu, B. Li, M. Zhou, A. Wing-Keung Law, K. Zhou, *ACS Appl. Mater. Interfaces* **2019**, *11*, 40564.
[50] W. D. Jung, J.-S. Kim, S. Choi, S. Kim, M. Jeon, H.-G. Jung, K. Y. Chung, J.-H. Lee, B.-K. Kim, J.-H. Lee, H. Kim, *Nano Lett.* **2020**, *20*, 2303.
[51] H. D. Lim, H. K. Lim, X. Xing, B. S. Lee, H. Liu, C. Coaty, H. Kim, P. Liu, *Adv. Mater. Interfaces* **2018**, *5*, 1701328.
[52] Y. Wang, H. Hao, K. G. Naik, B. S. Vishnugopi, C. D. Fincher, Q. Yan, V. Raj, H. Celio, G. Yang, H. Fang, Y.-M. Chiang, F. A. Perras, P. Jena, J. Watt, P. P. Mukherjee, D. Mitlin, *Adv. Energy Mater.* **2024**, *14*, 2304530.
[53] J. E. Lee, K.-H. Park, J. C. Kim, T.-U. Wi, A. R. Ha, Y. B. Song, D. Y. Oh, J. Woo, S. H. Kweon, S. J. Yeom, W. Cho, K. Kim, H.-W. Lee, S. K. Kwak, Y. S. Jung, *Adv. Mater.* **2022**, *34*, 2200083.
[54] A.-K. Hatz, R. Calaminus, J. Feijoo, F. Treber, J. Blahusch, T. Lenz, M. Reichel, K. Karaghiosoff, N. M. Vargas-Barbosa, B. V. Lotsch, *ACS Appl. Energy Mater.* **2021**, *4*, 9932.
[55] F. Marchini, B. Porcheron, G. Rousse, L. Albero Blanquer, L. Droguet, D. Foix, T. Koç, M. Deschamps, J. M. Tarascon, *Adv. Energy Mater.* **2021**, *11*, 2101111.
[56] M. Liao, E. Cao, D. Julius, Y. Cheng, *Nature* **2013**, *504*, 107.
[57] P. Bron, S. Dehnen, B. Roling, *J. Power Sources* **2016**, *329*, 530.
[58] D. H. S. Tan, Y. S. Meng, J. Jang, *Joule* **2022**, *6*, 1755.
[59] Y.-S. Jo, J.-W. Hong, I.-H. Choi, J. Sung, J.-H. Park, H. Park, D. Kim, B. G. Kim, Y.-C. Ha, J. Seo, W.-Y. Chung, K.-J. Baeg, J.-W. Park, *Green Chem.* **2023**, *25*, 1473.
[60] I.-H. Choi, E. Kim, Y.-S. Jo, J.-W. Hong, J. Sung, J. Seo, B. Gon Kim, J.-h. Park, Y.-J. Lee, Y.-C. Ha, D. Kim, J. Hong Lee, J.-W. Park, *J. Ind. Eng. Chem.* **2023**, *121*, 107.
[61] J. Sung, H. G. Lee, Y.-S. Jo, D.-H. Kim, H. Park, J.-H. Park, D. Kim, Y.-C. Ha, K.-J. Baeg, J.-W. Park, *Energy Storage Mater.* **2024**, *67*, 103253.
[62] H. J. Kitchen, S. R. Vallance, J. L. Kennedy, N. Tapia-Ruiz, L. Carassiti, A. Harrison, A. G. Whittaker, T. D. Drysdale, S. W. Kingman, D. H. Gregory, *Chem. Rev.* **2014**, *114*, 1170.
[63] E. Sarbu, I. Călinescu, *UPB Sci. Bull. B* **2014**, *76*, 95.
[64] A. T. S. Freiberg, J. Sicklinger, S. Solchenbach, H. A. Gasteiger, *Electrochim. Acta* **2020**, *346*, 136271.
[65] J. Vogel, M. Sacchi, *J. Electron Spectrosc. Relat. Phenom.* **1994**, *67*, 181.